A New Robust Nonlinear Control Strategy for UIPC in Isolated Hybrid Microgrids

Zolfaghari, Mahdi ; B. Gharehpetian, Gevork; Blaabjerg, Frede; Anvari-Moghaddam, Amjad

Published in:
International Journal of Electrical Power & Energy Systems

DOI (link to publication from Publisher):
10.1016/j.ijepes.2023.109569

Publication date:
2024

Document Version
Publisher's PDF, also known as Version of record

Electrical Power and Energy Systems 155 (2024) 109569

Contents lists available at ScienceDirect

International Journal of Electrical Power and Energy Systems

journal homepage: www.elsevier.com/locate/ijepes

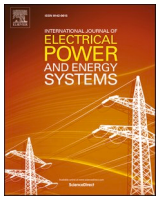

A new robust nonlinear control strategy for UIPC in isolated hybrid microgrids

Mahdi Zolfaghari [a], Gevork.B. Gharehpetian [a], Frede Blaabjerg [b], Amjad Anvari-Moghaddam [b,*]

[a] Department of Electrical Engineering, Amirkabir University of Technology, Tehran, Iran
[b] Department of Energy (AAU Energy), Aalborg University, 9220 Aalborg, Denmark

ARTICLE INFO

Keywords:
Isolated hybrid microgrid
UIPC
Nonlinear control

ABSTRACT

This paper focuses on the control of unified interphase power controller (UIPC) in isolated hybrid microgrids (HmGs), where the UIPC is used as the main component for interconnecting of AC and DC sub-grids. The investigated HmG encompasses two AC sub-grids and one purely storage DC sub-grid (PSDC) and multiple adjustable loads. A robust nonlinear model reference adaptive control (NMRC) strategy is offered for controlling the UIPC, keeping an acceptable two-way power exchange control with uncomplicated topology. Further, a novel configuration for the DC link power converter is suggested using the dual-active-bridge topology. Also, a harmonic-based modeling method is used to model the UIPC's power converter. The proposed configuration provides bidirectional power flow, increased power density, straightforward adaptation of zero-voltage switching, and direct access to cascading and parallelism to increase the ratings and reliability of UIPC. The simulation results illustrate the feasibility of the suggested topology for isolated HmGs.

1. Introduction

According to the recent studies, hybrid microgrids (HmGs) are suitable candidates to interconnect several AC and DC sub-grids because HmGs have inherit feature of reducing AC to DC transformation units, furnish overall handling of multiple sub-grids, and simplify the combination of these sub-grids with conventional power grid [1–4]. In general, there are multiple sub-grids within a typical HmG which are typically intertied with each other using interlink converters. This interconnection is necessary for the sub-grids because it lets the sub-grids to exchange active and reactive power in essential conditions to preserve frequency and/or voltage stability. This way, the isolated HmG could preserve the operational limits and provides the loads a reliable connection [5–9].

As the early first solution to interconnect AC and DC sub-grids, a single AC/DC power converter (SIPC) has been suggested by the researchers. For this purpose, different bridge-type structures have been used with sophisticated control schemes [10–12]. For instance, in [13], the authors have used a topology to embed an energy storage (ES) unit on the DC side; while interconnecting AC and DC sides. This resulted in more stability of whole HmG during transitions. However, the control of DC side becomes more challenging. In [14], Γ-Z-Source-based SIPC has been used in HmG structure. The main merit of this topology lies in its higher reliability and efficiency when compared to the traditions SIPC. The authors in [15] have presented a back-to-back structure to join HmGs. This is a multi-port topology which integrates AC and DC resources into one power electronics-based controlled block. As the SIPC-based topology limits the amount of exchanged power between the DC and AC sides, many researchers have suggested the parallel power converters (PAPCs) configuration in HmGs. The parallel connection also results in higher reliability. Nevertheless, application of such connections results in many problems and challenges in power and frequency control of intertied sub-grids. For instance, the control scheme must be able to remove the circulating current between PAPCs through regulating the output voltage of each SIPC in a coordinated manner. In order to overcome these problems, many techniques and strategies have been proposed. For example, authors of [16] have investigated the possibility of arranging the method of [14] into a parallel configuration for Γ-Z-Source units. Then, they have proposed a modified control method to reduce the effects of active power and voltage fluctuations of the DC side on the sub-grid's stability. The researchers in [17] have studied the effectiveness of the traditional droop-based control method in management of a typical HmG. As a follow-up to this work, the authors in [18] have tried to adapt the virtual droop theory into the control

* Corresponding author at: Pontoppidanstræde 111, 9220 Aalborg, Denmark.
E-mail address: aam@energy.aau.dk (A. Anvari-Moghaddam).

https://doi.org/10.1016/j.ijepes.2023.109569
Received 21 August 2022; Received in revised form 8 August 2023; Accepted 13 October 2023
Available online 18 October 2023

structure of a HmG in order to increase the power management performance of HmG. With the purpose of removing the problems raised by PAPCs, some researches have proposed some solutions using solid state transformer (SST), energy router-based structure (ERS), and sophisticated small adjustable AC transmission system (FACTS) devices. For example, in [19], an SST has been used to intertie AC and DC sub-grids. In comparison to traditional transformers, the SST removes the inductive elements which impose considerable losses to the power systems. The SST also enjoys the merits of power electronics-based control blocks which enables the operator to control the power exchange in an adjustable way. Accordingly, the SST has been used in [19] and [20] to integrate several low-and medium-voltage HmGs. The concept of ERS has been proposed in [21] to accommodate several AC and DC microgrids with reduced conversion units. The ERS provides a multi-port-like configuration which lets the AC and DC blocks to add-up with the power grid. The cost-effective feature of this structure is its main merit but the relatively high input voltages and output currents relaxation are the main challenges of ERS. The FACTS-based configurations mainly include application of unified power flow controller (UPFC), unified power quality conditioner (UPQC), and more recently, unified interphase power controller (UIPC), have been suggested as a useful alternative to PAPCs to intertie HmGs. The UPFC has been applied in a HmG in [22] so that the DC sources have been connected to the DC side power converter and the power flow properties have been provided with the AC side and power grid. The UPQC has been addressed in [23] and [24] as an interconnecting element for HmGs. The UPQC model has been changed so that it accepts the DC side voltage without stabilizing the power flow capability. The back-to-back PAPCs have been adopted and therefore, this structure may have some problems the same as PAPC-based HmGs. The work presented in [25], has used the UIPC to tie two AC sub-grids and one DC sub-grid. In the same study, the grid-tied operation of HmG has been verified and the sub-grids have been capable of interacting with each other so that the power flow from one sub-grid to another one has been provided in emergency conditions. The power grid has been responsible for providing voltage and frequency control and guaranteed the stability of the sub-grids. In [26], the authors have developed the application of UIPC in coupling several sub-grids and again, it has been assumed that the HmG is connected to the power grid. The main advantages of UIPC in application HmG include adjustable active and reactive power flow control, fault-protected feature, reducing multiple conversion units, enhanced reliability and increased power transfer capacity.

Until now, to the best of authors' knowledge, the feasibility of isolated HmGs with the UIPC as its main interconnection element has not been probed yet. Accordingly, the current paper focuses on investigating the stable operation of isolated HmGs. The main novelties and highlights of this work are as follows:

- A novel topology for the DC side power conversion unit of UIPC based on the dual-active-bridge structure is proposed.
- A new control strategy based on robust nonlinear model reference adaptive control (NMRC) concept, is developed for UIPC.
- The harmonic-based modeling method is used to model the UIPC's power converter in order to facility in design paradigm.
- The proposed configuration provides bidirectional power flow, increased power density, straightforward adaptation of zero-voltage switching, and direct access to cascading and parallelism to increase the ratings and reliability of UIPC.

The remainder sections of the current work are outlined as follows: The novel topology for UIPC and modelling process are described in Section 2. The new NMRC-based control strategy is presented in Section 3. Further, Section 4 discusses the simulation results and finally, inferencing remarks are given in Section 5.

2. Modeling of HmG and new UIPC configuration

As shown in Fig. 1, a common HmG encompassing two AC sub-grids and one purely storage DC sub-grid (PSDC) is considered in this paper. The HmG is isolated from the main power grid and AC sub-grids and AC PSDC are intertied using UIPC. There are some renewable resources, as seen in Fig. 1, wind turbine and PV system, in the AC sub-grids and also some energy storage system (ESS) and adjustable and non-adjustable loads. The PV system in the right-sided AC sub-grid is coupled with the AC bus using DC/DC and DC/AC interfaces. There are one ESS and one non-adjustable load in this sub-grid. The ESS in this sub-grid is essential to compensate the power shortage in the AC sub-grid when no power can be transferred from the other AC sub-grid or the PSDC. Nevertheless, the ESSs in the AC sub-grids can provide some of the demand in this study to further regulate the voltage and frequency in these sub-grids. The PSDC contains a cluster of ESSs. The main duty of an energy management system (EMS) is to provide a whole observation of the HmG operational conditions and providing appropriate reference signals to the sub-grids control systems to determine timely control actions. The ESSs in the PSDC are rechargeable and thus can contribute in power exchange between sub-grids when needed. It should be noticed that the left-sided AC sub-grid contains an adjustable-load which can vary its power consumption based on the UIPC signals and EMS commands. The details of this load model are described in [27].

2.1. New UIPC structure

To allocate the PSDC in the HmG environment using the UIPC, we suggest a novel topology for DC power conversion unit of the UIPC, as demonstrated in Fig. 2. As shown, the per-phase model encompasses two major sections: series power converter (SEPC) and parallel power converter (PAPC). To control the exchanged power between the two AC sub-grids, the SEPC add a tunable series voltage into the tie line through power transformer T_{SPC}. The voltage at AC bus of each AC sub-grid is named as V_{AC}^{1} and V_{AC}^{2}, respectively. In the UIPC topology, each phase encompasses one SEPC, labeled by $SEPC_i$, $i = 1, 2, 3$. The PAPC targets on adjusting the voltage of DC link. Besides, it manages the two-way power exchange control in collaboration with the ESSs main power converters (MAC). As shown in Fig. 2, the ESSs in the DC sub-grid are coupled to the DC link through MAC. This converter along with the voltage multiplier and the high-frequency transformer (HFT), construct a dual-active-bridge structure. The MAC is coupled with the PSDC sub-grid straightly and, in this paper, a new control strategy based on NMRC concept is proposed to appropriately control the MAC, as presented in Section III. The HFT carries out two major roles; (1) it yields a voltage isolation using galvanic property, and (2) it enhances amplifying factors of the conversion unit with a lower cost in comparison with the conventional topology. Nevertheless, if the control system of this structure is not designed appropriately, the efficiency of this structure may be reduced due to circulating current. Accordingly, to remove this barrier, the NMRC is suggested in this paper. It is worth mentioning that there is one PAPC for all three phases. The UIPC operates in two modes according to the power flow direction; capacitive or inductive. The switches S_1 and S_2 are able to conduct the current in forward and reverse directions and operate in on-or-off states according to the UIPC mode to provide correct power flow direction.

2.2. Order reduction of proposed model

The first step in designing the NMRC controller is determining the dynamics of the plant model. In the topology demonstrated in Fig. 2, a three-phase neutral point-clamped (NPC) structure is implemented for the multiplier and is coupled with the HFT. This unit is used to scale down the proportion of HFT windings. For the PAPC unit, a three-phase full-bridge NPC is used. Because the DC link must be able to exchange

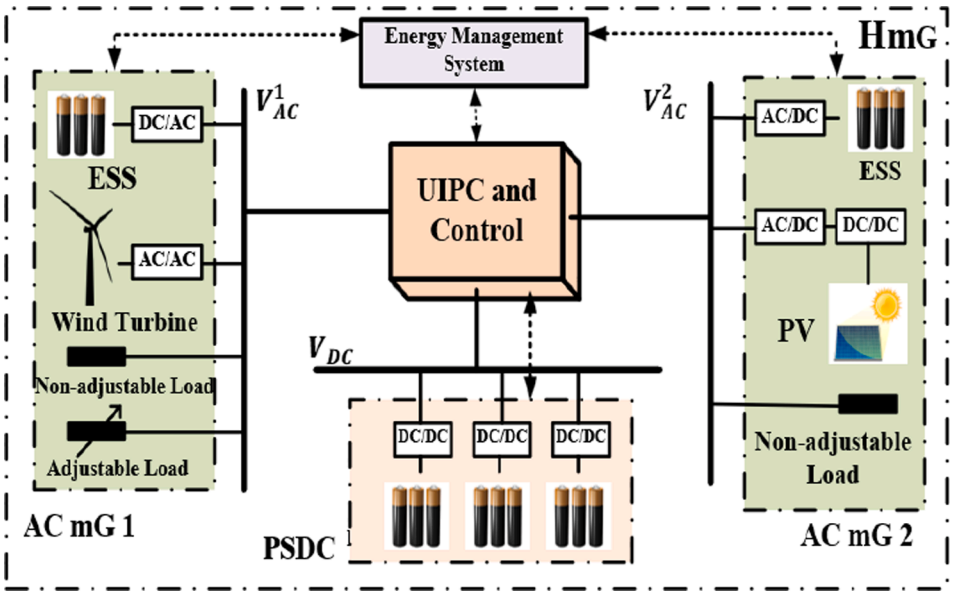

Fig. 1. A typical HmG configuration considered in this paper: two AC sub-grids and on DC sub-grids are intertied using UIPC.

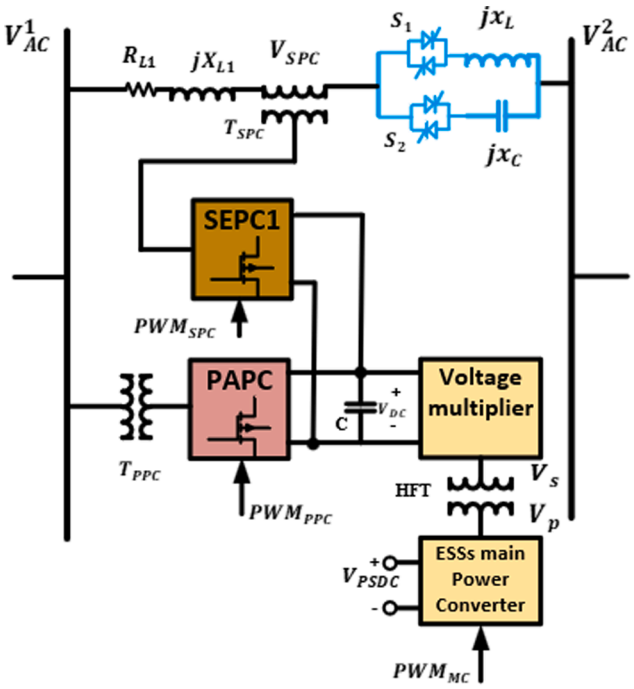

Fig. 2. Proposed UIPC topology.

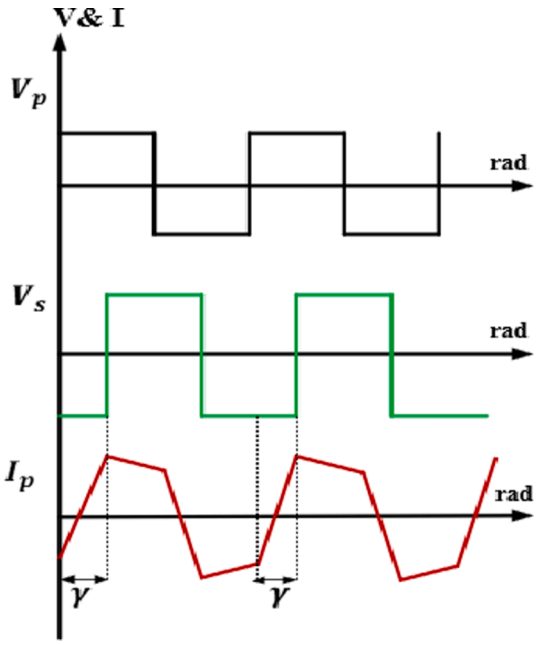

Fig. 3. The voltages and current of HFT.

power with the AC side, all switches are bidirectional. In order to generate the voltages V_p and V_s, which are the primary and secondary voltages of the HFT, the square pulse of half duty cycle control mechanism is used. These voltages are displaced by γ with respected to the power exchange direction.

Therefore, the transferred power is as follows:

$$P_{ex} = a_N\left(\left(V_p V_s \gamma(\pi - |\gamma|)\right)/2\pi\omega L_1\right) \tag{1}$$

where a_N is the proportion of HFT and L_1 is the inductance of the transmission line and the inductance among HTF and output of MAC. Fig. 3 shows the primary and secondary voltages and also the input current of HTF regarded in the modelling procedure according to (1).

If the switches of the proposed dual-bridge-based structure are functioned by an instantaneous scheme, i.e., at each time one of the switches in a power converter leg is on and the other one is off, the harmonic-based modelling concept could be adopted by using Fourier transformation to the switching function as follows:

$$S(t) = 1\Big/2 + 2\Big/\pi\left(\sum_{k=0}^{\infty}\left(\sin\left((2k+1)(\omega_s t - \varphi_j)\right)\right)\Big/(2k+1)\right),\ j = 1,\cdots,4 \tag{2}$$

where ω_s in rad/s is the switching frequency and φ_j is the delay of the pulse in relation to a desired reference frame.

Regarding the switching function (2), we can write the voltages V_p and V_s as:

$$V_p(S(t)) = V_{PSDC}[S_1(t) - S_2(t)] \tag{3}$$

$$V_s(S(t)) = V_{DC}/2[S_3(t) - S_4(t)] \tag{4}$$

where V_{PSDC} is the voltage at the DC common bus of PSDC, V_{DC} is the capacitor voltage, and $S_1(t)$ and $S_2(t)$ are the switching functions. In the modeling procedure, the duty cycle is 0.5 considering the square wave switching scheme. Therefore, $S_2(t)$ is the complement of $S_1(t)$ and we obtain $\varphi_2 = \pi + \varphi_1$, and in a similar approach, $\varphi_4 = \pi + \varphi_3$. Also, setting $\varphi_1 = 0$ then $\varphi_3 = \gamma$. therefore, (3) and (4) become:

$$V_p(t) = V_{PSDC}\left(4\Big/\pi\left(\sum_{k=0}^{\infty} sin((2k+1)\omega_s t)\Big/(2k+1)\right)\right) \tag{5}$$

$$V_s(t) = V_{DC}\Big/2\left(4\Big/\pi\left(\sum_{k=0}^{\infty} \sin((2k+1)\omega_s t - \gamma)\Big/(2k+1)\right)\right) \tag{6}$$

Based on Kirchhoff's voltage law, in the primary winding of HFT we can write:

$$\begin{aligned} V_p(t) - a_N V_s(t) &= R_1 I_p(t) + L_1 \frac{dI_p(t)}{dt} \\ &= V_{PSDC}\left(4\Big/\pi\left(\sum_{k=0}^{\infty} sin((2k+1)\omega_s t)\Big/(2k+1)\right)\right) - a_N V_{DC}\Big/2\left(4\Big/\pi\sum_{k=0}^{\infty} sin((2k+1)\omega_s t)\Big/(2k+1)\right) \end{aligned} \tag{7}$$

Simply using the Laplace transform of infinite time series and knowing that The Laplace transform of a signal $x(t)$ is equivalent to the Fourier transform of the signal $x(t)e^{-\sigma t}$ (the Fourier transform is equivalent to the Laplace transform evaluated along the imaginary axis of the s-plane), we have the following expression:

$$I_p(s) = 1\Big/(R_1 + L_1 s)\left(V_{PSDC}\left(4\Big/\pi \times L\left(\sum_{k=0}^{\infty} sin((2k+1)\omega_s t)\Big/(2k+1)\right)\right) - a_N V_{DC}\Big/2\left(4\Big/\pi \times L\left(\sum_{k=0}^{\infty} sin((2k+1)\omega_s t)\Big/(2k+1)\right)\right)\right)$$

Using the inverse Laplace and knowing that the inverse Laplace of a function like $\frac{1}{s+a}$ is e^{-at}, we have:

$$I_p(t) = 4\Big/\pi\sum_{k=0}^{\infty} 1\Big/(2k+1)(V_{PSDC}/\varkappa(k)sin((2k+1)\omega_s t - \varphi_{\varkappa(k)}) - a_N V_{DC}/2|\varkappa(k)|sin((2k+1)\omega_s t - \varphi_{\varkappa(k)}))) \tag{8}$$

where $|\varkappa(k)| = \left(R_1^2 + ((2k+1)\omega_s L_1)^2\right)^{1/2}$ and $\varphi_{\varkappa(k)} = tan^{-1}((2k+1)\omega_s L_1/R_1)$.

According to Kirchhoff's current law, the current of output capacitor is given as follows:

$$C\Big/2\frac{dV_{DC}}{dt} = I_s - I_{dc} = a_N I_p[S_3(t) - S_4(t)] - V_{DC}\Big/R_{out} \tag{9}$$

Rearranging and simplifying (9) one obtains:

$$\begin{aligned} \frac{d}{dt}(V_{DC}) &= h(V_{DC}(t), \gamma) \\ &= 16a_N\Big/C\pi^2\left(\sum_{k=0}^{\infty}1\Big/(2k+1)^2(V_{PSDC}/\varkappa(k)cos((2k+1)\gamma - \varphi_{\varkappa(k)}) - a_N V_{DC}/|\varkappa(k)|cos(\varphi_{\varkappa(k)}))\right) - 2V_{DC}\Big/CR_{out} \end{aligned} \tag{10}$$

Since commonly we have $\omega_s L_1 \gg R_1$, thus, $\varphi_{\varkappa(k)} \cong \pi/2$. Therefore, we can have:

$$\frac{d}{dt}(V_{DC}) = h(V_{DC}(t)) + Qu \tag{11}$$

In which $h(V_{DC}(t)) = -2V_{DC}/CR_{out} = -\rho V_{DC}$, $Q = 16a_N/C\pi^2\left(\sum_{k=0}^{\infty}1/(2k+1)^2(V_{ESDC}/\varkappa(k))\right)$, and $u = sin((2k+1)\gamma)$. Accordingly, this first order transfer function is used to design the NMRC control scheme in the subsequent section.

3. Proposed nonlinear MRC-based control of UIPC with enhanced robustness

In order to stabilize the HmG in isolated mode, the frequency and voltage of each AC sub-grid and voltage of DC link of UIPC should be controlled through appropriate power exchange control between the sub-grids through UIPC. To this end, a novel control strategy is presented in this section to manage the HmG power exchange among the sub-grids through the control loops of UIPC. We set the DC side voltage free from power exchange oscillation effects by designing the nonlinear MRAC-based robust control scheme.

3.1. Overall configuration of New HmG management strategy and UIPC control

Fig. 4 demonstrates general structure of the proposed control strategy for UIPC. As demonstrated, there are three control blocks for SEPC, PAPC, and MAC, respectively. Also, there is an EMS unit which observes the conditions of the sub-grids; carrying out necessary reference signal calculations for the sub-grids according to the feedback signals from the sub-grids and user-specified reference values.

3.2. Controller design using NMRC strategy

For a standard system model described as follows:

$$\frac{d}{dt}(x(t)) = Ax(t) + B(u(t) + \mathfrak{V}(x,t)) \tag{12}$$

where $x(t) \in \mathscr{R}^n$ is the system state, $u(t) \in \mathscr{R}$ is the system control input, $\mathfrak{V}(x,t) : \mathscr{R} \times \mathscr{R}^n \to \mathscr{R}$ demonstrates time-and-state dependent disturbances which may be considered as uncertainty or unmodeled dynamics of the system, and the matrices $A \in \mathscr{R}^{n\times n}$ and $B \in \mathscr{R}^n$ are assumed to be a controllable pair described as (A,B).

We introduce a reference model as follows:

$$\frac{d}{dt}\left(x_{ref}(t)\right) = A_{ref}x_{ref}(t) + B_{ref}u_{ref}(t) \tag{13}$$

where $A_{ref} \in \mathscr{R}^{n\times n}$ is Hurwitz and determinable, $B_{ref} \in \mathscr{R}^n$ is a known matrix, and $u_{ref}(t) \in \mathscr{L}_\infty$ is the reference control signal.

According to NMRC concept, the reference model should be assigned so that the following condition is achieved:

$$A_{ref} = A + B\rho_x^T \tag{14}$$

$$B_{ref} = B\rho_r \tag{15}$$

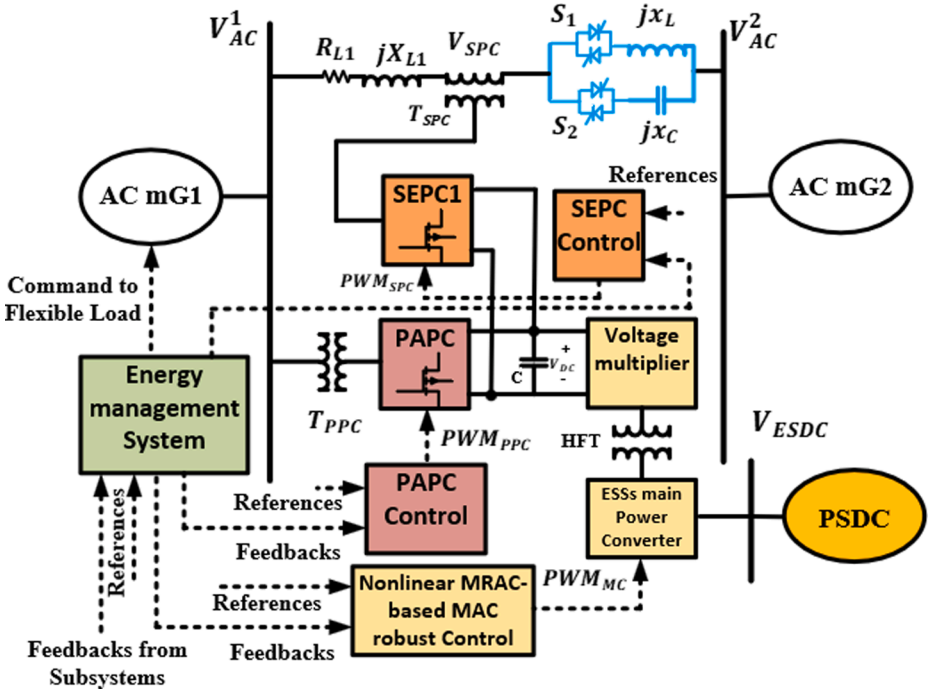

Fig. 4. Overall configuration new UIPC control strategy for adopting in HmG.

where $\rho_x \in \mathscr{R}^n$ and $\rho_r \in \mathscr{R}\{0\}$ are undetermined values that provide the control performance so that $\mho \equiv 0$.

Accordingly, the objective of control design is to determine the control law $u(t)$ so that the perturbed system (12) behaves similar to the reference model (13), without information about the system parameters and in the presence of time-and-state dependent disturbance $\mho(x,t)$.

The design steps are as follows:

Step 1. Rewrite the perturbed system (12) using (13) as follows:

$$\frac{d}{dt}(x(t)) = A_{ref}x(t) + B_{ref}\rho_r^{-1}\left(u(t) + \mho(x,t) - \rho_x^T x(t)\right) \tag{16}$$

Step 2. The nonlinear control law and adaptation paradigm are described as follows:

$$u(t) = \hat{\rho}_r r + \hat{\rho}_x^T x(t) + \hat{\rho}_r K^T \mathscr{g}(\tilde{x}(t)) \tag{17}$$

$$\frac{d}{dt}(\hat{\rho}_r) = -k_1^{-1}\sigma(\tilde{x}(t), r)\left(\tilde{x}^T(t)P + \mathscr{g}^T(\tilde{x}(t))\Lambda\right)B_{ref} \tag{18}$$

$$\frac{d}{dt}(\hat{\rho}_x) = -K_2^{-1}x(t)\left(\tilde{x}^T(t)P + \mathscr{g}^T(\tilde{x}(t))\Lambda\right)B_{ref} \tag{19}$$

where $k_1 > 0$, $K_2^T = K_2$, $K_2 > 0, K_2 \in \mathscr{R}^{n\times n}$, $K = \left[k_3^T \;\; k_4^T \;\; k_5^T\right]^T \in \mathscr{R}^{3n}$, $P^T = P$, $P \geq 0$, $P \in \mathscr{R}^{n\times n}$, $\Lambda = [\Lambda_0 \;\; \Lambda_1 \;\; \Lambda_2]^T$ with $\Lambda_j = diag\{\lambda_{ij}\}$, $\lambda_{ij} \in \mathscr{R}_+$, $i = 1, 2, \cdots, n$, $j = 0, 1, 2$, $\mathscr{g}(\tilde{x}(t)) = \left[\mathscr{g}_0^T(\tilde{x}(t)) \;\; \mathscr{g}_1^T(\tilde{x}(t)) \;\; \mathscr{g}_2^T(\tilde{x}(t))\right]^T$, $\mathscr{g}_0(\tilde{x}(t)) = [\tilde{x}(t)]^0$, $\mathscr{g}_1(\tilde{x}(t)) = [\tilde{x}(t)]^\zeta$, $\mathscr{g}_2(\tilde{x}(t)) = [\tilde{x}(t)]^\eta$, $\zeta \in (0,1)$, $\eta > 1$, $\sigma(\tilde{x}(t), r) = r + K^T\mathscr{g}(\tilde{x}(t))$, $\tilde{x}(t) = x(t) - x_{ref}(t)$.

Step 3. According to (17)–(19), the closed-loop dynamics are obtained as follows:

$$\frac{d}{dt}(x(t)) = A_{ref}x(t) + B_{ref}\left[\sigma(\tilde{x}(t), r)(1 + \tilde{\psi}_1) + \tilde{\psi}_2 x(t) + \overline{v}(t, x(t))\right] \tag{20}$$

where the disturbance is $\overline{v}(t, x(t)) = \rho_r^{-1}v(t, x(t))$ which is time-and-state dependent and the approximation gains are as follows:

$$\tilde{\psi}_1 = \rho_r^{-1}\hat{\rho}_r - 1 \tag{21}$$

$$\tilde{\psi}_2 = \rho_r^{-1}\left(\hat{\rho}_x^T - \rho_x^T\right) \tag{22}$$

and thus, the errors dynamics are as follows:

$$\frac{d}{dt}(\tilde{x}(t)) = A_{ref}\tilde{x}(t) + B_{ref}\left[K^T\mathscr{g}(\tilde{x}(t)) + \tilde{\psi}_1\sigma(\tilde{x}(t), r) + \tilde{\psi}_2 x(t) + \overline{v}(t, x(t))\right] \tag{23}$$

$$\frac{d}{dt}(\tilde{\psi}_1) = -\rho_r^{-1}k_1^{-1}\sigma(\tilde{x}(t), r)\left(\tilde{x}^T(t)P + \mathscr{g}^T(\tilde{x}(t))\Lambda\right)B_{ref} \tag{24}$$

$$\frac{d}{dt}(\tilde{\psi}_2) = -\rho_r^{-1}\left[-K_2^{-1}x(t)\left(\tilde{x}^T(t)P + \mathscr{g}^T(\tilde{x}(t))\Lambda\right)B_{ref}\right]^T \tag{25}$$

The stability of the closed-loop system can be proofed in the following steps:

Step 4. For a case in which $v(t, x(t)) \equiv 0$, the NMRC controller is applied to the system model. For $\zeta \in (0,1)$, $\eta > 1$, there exists $X^T = X > 0, X \in \mathscr{R}^{n\times n}$, $Y \in \mathscr{R}^{1\times n}$, $\mathscr{T} = diag\{\Im_i\} \geq 0$, $\mathscr{L}_j = diag\{\ell_j\} \geq 0$, for $i = 1, 2, \cdots, n$, $j = 0, 1, 2$, these linear matrix inequalities are feasible:

$$\widetilde{\mathbb{N}}_1 \leq 0, \;\; \mathscr{T} + \sum_{j=0}^{2}\mathscr{L}_j > 0 \tag{26}$$

$$1_n^T\left[\partial\left(B_{ref}Y + XA_{ref}^T\right) + \varpi\left(B_{ref}Y + XA_{ref}^T\right) + \mathscr{L}_0\right] \leq 0 \tag{27}$$

$$1_n^T\Big[(1+\eta)\partial\left(B_{ref}Y + XA_{ref}^T\right) + \eta\varpi\left(B_{ref}Y + XA_{ref}^T\right) + \varpi^T\left(B_{ref}Y + XA_{ref}^T\right) + (1+\eta)\mathscr{L}_1\Big] \leq 0 \tag{28}$$

$$1_n^T\Big[(1+\zeta)\partial\left(B_{ref}Y + XA_{ref}^T\right) + \zeta\varpi\left(B_{ref}Y + XA_{ref}^T\right) + \varpi^T\left(B_{ref}Y + XA_{ref}^T\right) + (1+\zeta)\mathscr{L}_2\Big] \leq 0 \tag{29}$$

where $\widetilde{\mathbb{N}}_1$ is given by (38).

Step 5. If the unmodeled dynamics are not negligible, i.e., for a case in which $\upsilon(t,x(t)) \neq 0$, then the following condition is preserved:

$$|\overline{\upsilon}|^2 \leq \upsilon^+ + \beth\|\widetilde{x}\|^2 + \beth_1\|\widetilde{x}\|^{2+\zeta} + \beth_2\|\widetilde{x}\|^{2+\eta} \tag{30}$$

where $\beth$, $\beth_1$, and $\beth_2 \in \mathscr{R}$ are positive bounded values.

The NMRC controller is applied to the system model and the following linear matrix inequalities are feasible:

$$\widetilde{\mathbb{N}}_2 \leq 0 \tag{31}$$

$$1_n^T\left[\partial\left(B_{ref}Y_0 + XA_{ref}^T\right) + \varpi\left(B_{ref}Y_0 + XA_{ref}^T\right) + \mathscr{L}_0\right] \leq 0 \tag{32}$$

$$1_n^T\Big[(1+\eta)\partial\left(B_{ref}Y_1 + XA_{ref}^T\right) + \eta\varpi\left(B_{ref}Y_1 + XA_{ref}^T\right) + \varpi^T\left(B_{ref}Y_1 + XA_{ref}^T\right) + (1+\eta)\mathscr{L}_1\Big] \leq 0 \tag{33}$$

$$1_n^T\Big[(1+\zeta)\partial\left(B_{ref}Y_2 + XA_{ref}^T\right) + \zeta\varpi\left(B_{ref}Y_2 + XA_{ref}^T\right) + \varpi^T\left(B_{ref}Y_2 + XA_{ref}^T\right) + (1+\zeta)\mathscr{L}_2\Big] \leq 0 \tag{34}$$

$$\mathscr{T} - \mu\beth I_n + \sum_{b=1}^{2} 2\mathscr{L}_b - \mu\beth_b I_n + \mathscr{L}_0 > 0 \tag{35}$$

$$\mathscr{T} \geq \mu\beth I_n \tag{36}$$

$$2\mathscr{L}_b - \mu\beth_b I_n \geq 0, b = 1,2 \tag{37}$$

and $\widetilde{\mathbb{N}}_2$ is given by (39).

Fig. 5 shows the structure of the proposed control system, outlined based on NMRC strategy. As demonstrated, a model is considered as the "reference model" to provide the desired output $y_{ref}(t)$ based on the received input $u_{ref}(t)$. Then, the error signal $e(t)$ is passed to the "nonlinear adaptation law" block to approximate $\widehat{\rho}_r$ and $\widehat{\rho}_x$. After that, the control signal $u(t)$ is produced by the "controller" block and is given to the plant model "MAC".

Considering the actual plant model, ΔV_{DC} is adopted to be the output signal $y(t)$. For the DC side voltage control, a droop curve is used as demonstrated in Fig. 6 in which $P_{ESS,Nom}$ and $V_{DC,Nom}$ are respectively the rated DC power of ESSs and DC side voltage, and α_{dp} is the droop factor. According to this characteristic, the DC side voltage decreases for positive power exchange and increases for the negative power exchange direction. This way, this characteristic provides a controllable power exchange paradigm while keeping the DC voltage in stable region.

Step 6. Considering the changes of the DC link voltage as the system output, the desirable reference would be $y_{ref}(t) = 0$ in Fig. 5. We consider the unmodeled dynamics as a function of changes in DC voltage and called Disturbance Factor (DF) here. This way, the unmodeled

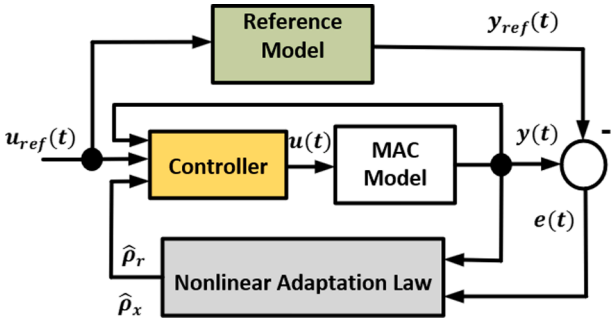

Fig. 5. Proposed NMRC control of MAC converter.

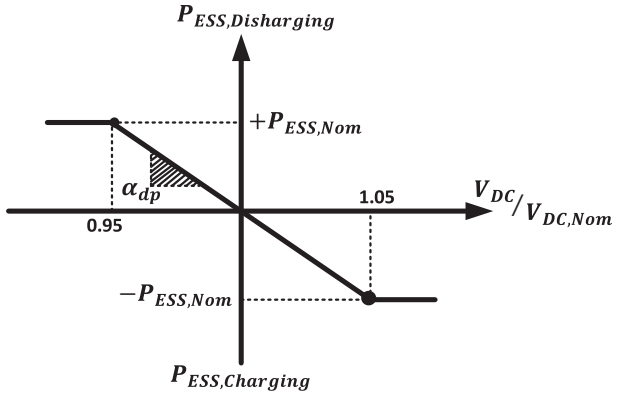

Fig. 6. Implemented droop pattern in the new control strategy.

dynamics is the nearest worst case since it directly affect the system output through the system states. The worst-case DFs set around DF = 1.5% and are not considered here because the worst case-based controller design makes the system overconservative through unwanted increased control effort. Nevertheless, the proposed algorithm is robust against the worst-case uncertainty as shown in Fig. 7. The stable operating points of the closed-loop system demonstrated in Fig. 5 for the proposed algorithm is analyzed in Fig. 7. The figure shows the bidirectional operation of the MAC power converter in both direct and reverse power flow directions for positive bounded, zero bounded, and negative bounded ranges of DF in percent. As shown, the most tolerable DF is about 1.4% which is in reverse power flow direction. The lowest DF value is 0.4% which is also in reverse direction. For the zero bounded, the DF is about 0.5% and the maximum value of DF for the direct power flow direction is found about 1.3%. All in all, the proposed algorithm provides the closed-loop system robust stability against the nearest worst-case DFs in the different operation modes of the HmG system.

$$\widetilde{\mathbb{N}}_1 = \begin{bmatrix} A_{ref}X + XA_{ref}^T + \mathscr{T} & 0 & 0 & 0 \\ * & B_{ref}Y + Y^TB_{ref}^T & B_{ref}Y + Y^TB_{ref}^T & B_{ref}Y + Y^TB_{ref}^T \\ * & * & B_{ref}Y + Y^TB_{ref}^T & B_{ref}Y + Y^TB_{ref}^T \\ * & * & * & B_{ref}Y + Y^TB_{ref}^T \end{bmatrix} \tag{38}$$

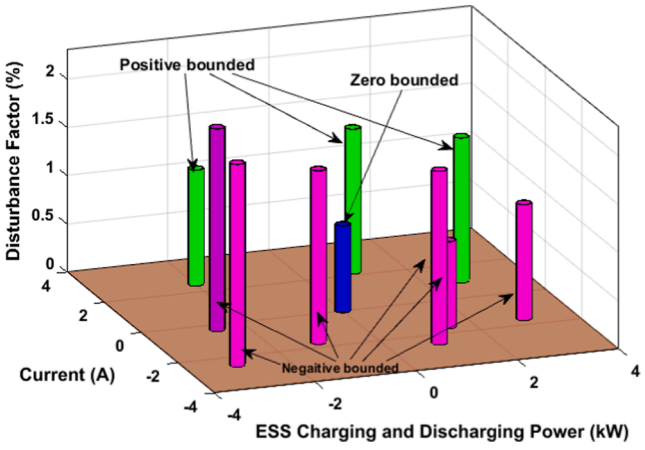

Fig. 7. Stable operation performance of the proposed ESS control system.

$$\widetilde{\mathbb{N}}_2 = \begin{bmatrix} A_{ref}X + XA_{ref}^T + \mathscr{T} & 0 & 0 & 0 & B_{ref} \\ * & B_{ref}Y_0 + Y_0{}^T B_{ref}^T + \frac{\mu v^+}{n}\Lambda_0^{-2} & B_{ref}Y_1 + Y_1{}^T B_{ref}^T & B_{ref}Y_2 + Y_2{}^T B_{ref}^T & B_{ref} \\ * & * & B_{ref}Y_1 + Y_1{}^T B_{ref}^T & B_{ref}Y_2 + Y_2{}^T B_{ref}^T & B_{ref} \\ * & * & 0 & B_{ref}Y_2 + Y_2{}^T B_{ref}^T & B_{ref} \\ * & * & 0 & * & -\mu I_n \end{bmatrix} \tag{39}$$

4. Simulation results

In order to validate the appropriateness of the new control structure, the results of simulation case studies using MATLAB are presented in this section. The simulated islanded HmG model is based on the configuration given by Fig. 1. It contains two AC sub-grids and one PSDC. Inside the first AC sub-grid, there is are 3×50 kW wind units, a 1×50 kW battery-based ESS, and some adjustable and non-adjustable loads. For the second AC sub-grid, a 1×250 kW PV unit and a 1×50 kW battery-based ESS, and on non-adjustable load are considered.

The PSDC includes 1×50 kW battery-based ESS which is able to sustain bidirectional DC power exchange using the dual-bridge topology equipped with the new NMRC-based control system. The specification of each PV module, wind turbine system and the battery are given in Tables 1–3. Note that in Table 1, STC and PTC respectively stands for Standard Test Condition (STC) and PVUSA Test Condition (PTC).

4.1. Power exchange performance evaluation and adjustable load response

To analyze the response of the adjustable loads to the control command, we assume that the non-adjustable load is 160 kW in the first AC sub-grid. The wind units generate 150 kW and therefore, the battery-based ESS is discharged to supply the demand. Nevertheless, the adjustable load with consumption pattern 20 kW : 20 kW : 80 kW (minimum 20 kW, maximum 80 kW, in 20 kW steps) can respond to the control command and increase its consumption to use the extra power provided by the battery-based ESS unit, likely, according to an agreement between adjustable load holder and the power market operator. Accordingly, as illustrated in Fig. 8, at t = 0.4 s, the consumed power in the first AC sub-grid is increased from 180 kW to 200 kW. Moreover, the dynamic response of the adjustable load to the new control system command is shown in Fig. 9. It is observed that the adjustable load has increased its demand from 20 kW to 40 kW. Also, the state of charge (SOC) of the battery-based ESS in the first AC sub-grid is demonstrated in Fig. 10. As shown, the battery has been in discharge mode until t = 0.4 s because the generated power of wind systems has not been enough to supply the extra 30 kW load power (20 kW of

Table 1
PV system module specification.

Power at STC (W)	415
Power at PTC (W)	385.2
Power Density at STC (W/m2)	192.13
Power Density at PTC (W/m2)	178.333
Vmp: Voltage at Max Power (V)	72.9
Imp: Current at Max Power (A)	5.69
Voc: Open Circuit Voltage (V)	85.3
Isc: Short Circuit Current (A)	6.09
Nominal Operating Cell Temp (°C)	45.8
Open Circuit Voltage Temp Coefficient (%/°C)	−0.229
Short Circuit Current Temp Coefficient (%/°C)	0.031
Max Power Temp Coefficient (%/°C)	−0.353

Table 2
Wind turbine system specifications.

Rated Power	50 kW
Maximum Output Power	54 kW
Generator	Direct-Drive Permanent Magnet Generator
Blade Quantity	3 Glass Fiber Blades
Rotor Blade Diameter	18.0 m (59.1 ft)
Start-up Wind Speed	3.0 m/s (6.7 mph)
Rated Wind Speed	10 m/s (22.3 mph)
Survival Wind Speed	59.5 m/s (133.1 mph)
Turbine Weight	6120 kg (13464.3 lbs)
Noise	58.5 db(A) @ 7 m/s
Temperature Range	−20 °C to +50 °C

Table 3
Battery system specifications.

Rated AC Power	50 kW
Maximum Power	55 kW
Input/ Output Voltage AC	400 V
Input/output Frequency	50 Hz
Out THDI	<3%
AC Current	72 A
Grid	3Phase 4Wires isolated line transformer
Operating Temperature Range	−4°F (−20 °C) to 104°F (40 °C)
Cell Chemistry	Lithium Iron Phosphate (LiFePO4)
Dimensions (W × D × H)	2250 × 1300 × 2591 mm
Min. Battery Efficiency	95%

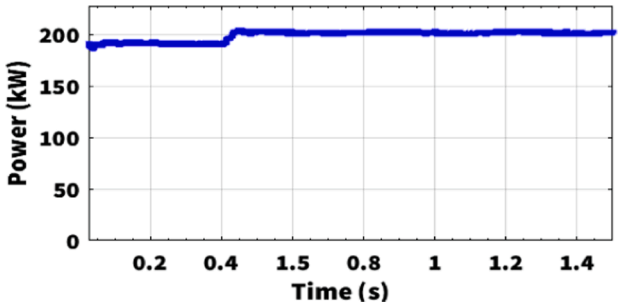

Fig. 8. The consumed power of the first AC sub-grid when the adjustable load varies its power consumption at t = 0.4 s.

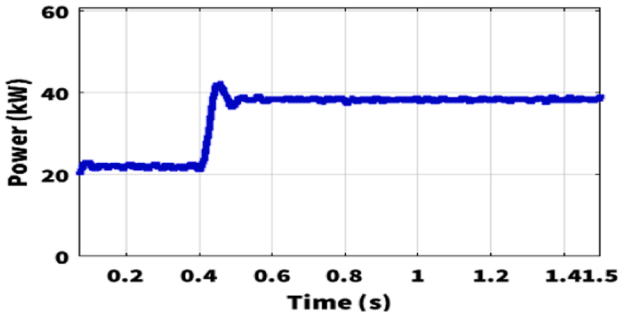

Fig. 9. The consumed power of adjustable load: it varies its consumption at t = 0.4 s.

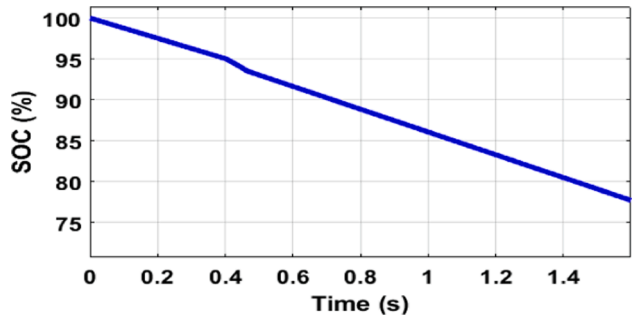

Fig. 10. The SoC of the battery-based ESS system in the first AC sub-grid when the adjustable load varies its power consumption at t = 0.4 s.

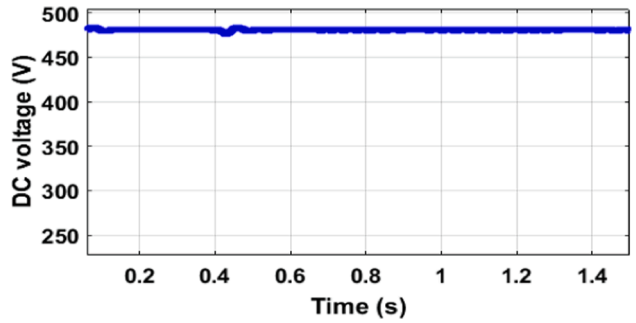

Fig. 11. The DC side voltage when the adjustable load varies its power consumption at t = 0.4 s.

minimum power of adjustable load +10 kW of the non-adjustable load). The adjustable load receives the control command at t = 0.4 s from the EMS and the proposed control structure to increase its power consumption by one 20 kW step. Therefore, it can be observed from Fig. 10 that the rate of discharge (RoD) of the battery-based ESS is increased. According to Fig. 10, the SoC battery discharges 20% in 1.4 s. For this to occur, a time gain constant can accelerate such response, as can be fulfilled in the Sheperd Model. More information can be found in [28].

Fig. 11 shows the DC side voltage in this condition. It is observed that the DC side control has been successful in managing and damping the voltage oscillations and keeping it at its rated value 480 V. The AC side voltage is 400 V (rms).

4.2. Optimal operation of ESSs with proposed NMRC algorithm

To analyze the performance of the HmG proposal in EFFECTIVE control of bidirectional power flow at ESSs bus, a comparative study is presented here. Accordingly, a step pulse with magnitude of 0.1 is

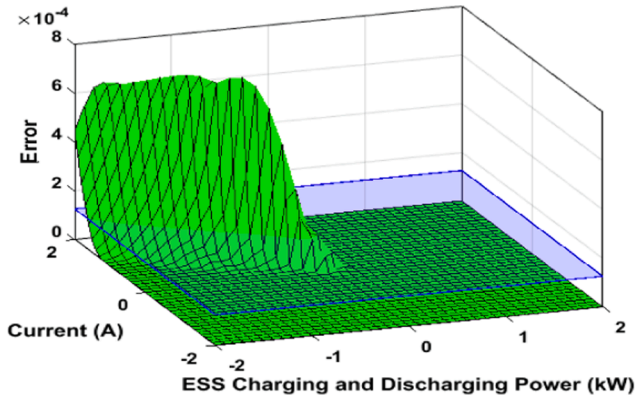

Fig. 12. Response of method of [29] to a step change in reference signal.

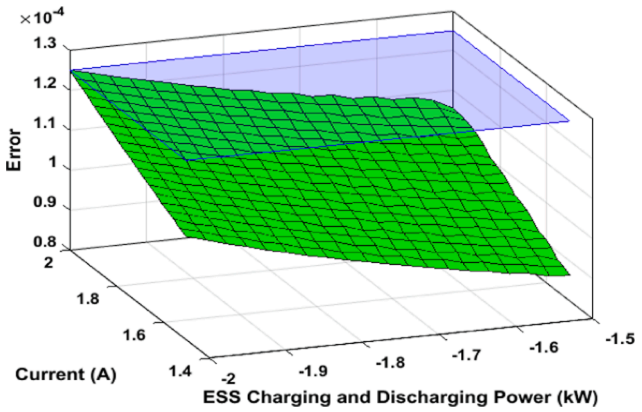

Fig. 13. Response of CMRAC method to a step change in reference signal.

applied to the DC bus reference control signal as a disturbance and the response of the proposed control structure is compared to the approaches followed by [29], and conventional model reference adaptive control (CMRAC). The error function minimization along with stable operation region and bidirectional flow capability are considered as the main properties for evaluation.

Fig. 12 shows the response of the method of [29] to the step disturbance. As illustrated, the ESSs can provide bidirectional power flow performance (positive and negative power and current signs) in a stable region. However, the maximum error magnitude is about 6.8×10^{-4}. For the sever disturbances, the absolute of error function may increase due to non-homogenized property and result in instability.

The result of simulation for the CMRAC method is demonstrated in Fig. 13. As observed, the maximum error magnitude is about 1.25×10^{-4}. However, the bidirectional power flow capability cannot be provided and the error function could not reach zero.

Considering the proposed method in this paper, the result is indicated in Fig. 14. In this case, the maximum error magnitude is about 1.22×10^{-4} with the bidirectional capability sustained. Also, in comparison to Fig. 12, the homogeneity of the error function is more observed and the stable operation region is extended.

5. Conclusion

The topology of power system would enjoy the advantages of the HmGs to integrate several AC and DC sub-grids. These sub-grids have commonly been intertied using the parallel power converters. Nevertheless, the traditional interconnection methods have raised several

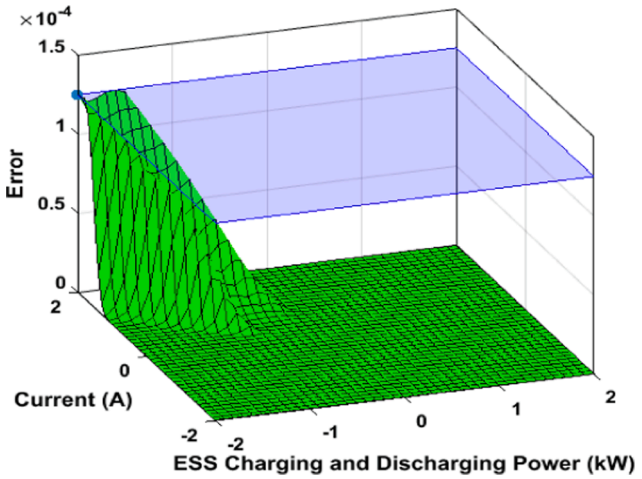

Fig. 14. Response of the proposed method to a step change in reference signal.

problems. To bridge the gaps, this paper has presented a new control paradigm based on NMRC algorithm. A new structure for UIPC was proposed which provided voltage isolation with reduced cost. The results endorsed that the new UIPC structure and control strategy are beneficial for isolated HmGs interconnected by UIPC; specifically, the NMRC method showed better performance in providing stable operation region and bidirectional flow capability in islanded HmGs interconnected by UIPC. Also, the appropriate coordination between adjustable loads and resources in power flow control was established by the proposed configuration and control method.

CRediT authorship contribution statement

Mahdi Zolfaghari: Conceptualization, Methodology, Software, Validation, Formal analysis, Investigation, Resources, Writing – original draft. **Gevork.B. Gharehpetian:** Conceptualization, Methodology, Formal analysis, Supervision, Writing – review & editing. **Frede Blaabjerg:** Methodology, Formal analysis, Writing – review & editing. **Amjad Anvari-Moghaddam:** Methodology, Formal analysis, Writing – review & editing.

Declaration of Competing Interest

The authors declare that they have no known competing financial interests or personal relationships that could have appeared to influence the work reported in this paper.

Data availability

Data will be made available on request.

References

[1] Chang J, Moon S, Lee G, Hwang P. A new local control method of interlinking converters to improve global power sharing in an islanded hybrid AC/DC microgrid. IEEE Trans Energy Convers 2020:1.
[2] Peng S, Lin X, Tang J, Xie K, Ponci F, Monti A, Li W. Probabilistic power flow of AC/DC hybrid grids with addressing boundary issue of correlated uncertainty sources. IEEE Trans Sustainable Energy 2022:1.
[3] Armghan H, Yang M, Armghan A, Ali N, Wang MQ, Ahmad I. Design of integral terminal sliding mode controller for the hybrid AC/DC microgrids involving renewables and energy storage systems. Int J Electr Power Energy Syst 2020;119:105857.
[4] Venkateswaran R, Yesudhas AA, Lee SR, Joo YH. Integral sliding mode control for extracting stable output power and regulating DC-link voltage in PMVG-based wind turbine system. Int J Electr Power Energy Syst 2023;144:108482.
[5] Feng F, Zhang P, Zhou Y, Wang L. Distributed networked microgrids power flow. IEEE Trans Power Syst 2022:1.
[6] Li X, Dong C, Jiang W, Wu X. Distributed dynamic event-triggered power management strategy for global economic operation in high-power hybrid AC/DC microgrids. IEEE Trans Sustainable Energy 2022:1.
[7] Ordono A, Unamuno E, Barrena JA, Paniagua J. Interlinking converters and their contribution to primary regulation: a review. Int J Electr Power Energy Syst 2019;111:44–57.
[8] Wang Y, Li Y, Cao Y, Tan Y, He L, Han J. Hybrid AC/DC microgrid architecture with comprehensive control strategy for energy management of smart building. Int J Electr Power Energy Syst 2018;101:151–61.
[9] Kumar K, Bae S. Dynamic power management based on model predictive control for hybrid-energy-storage-based grid-connected microgrids. Int J Electr Power Energy Syst 2022;143:108384.
[10] Zhao G, Jin L, Wang Y. Distributed event-triggered secondary control for islanded microgrids with disturbances: A hybrid systems approach. IEEE Trans Power Syst 2022:1.
[11] Yi X, Peng Y, Zhou Q, Huang W, Xu L, Shen J, Shuai Z. Transient synchronization stability analysis and enhancement of paralleled converters considering different current injection strategies. IEEE Trans Sustainable Energy 2022:1.
[12] Yao W, Wang Y, Xu Y, Dong C. Small-signal stability analysis and lead-lag compensation control for DC networked-microgrid under multiple time delays. IEEE Trans Power Syst 2022:1.
[13] Bose U, Chattopadhyay S, Chakraborty C. Topological investigation on interlinking converter in a hybrid microgrid. In: 2018 IEEE international conference on industrial electronics for sustainable energy systems (IESES); 2018. p. 62–7.
[14] Poursmaeil M, Dizgah SM, Torkaman H, Afjei E. Autonomous control and operation of an interconnected AC/DC microgrid with Γ-Z-Source interlinking converter. In: 2017 Smart Grid Conference (SGC); 2017. p. 1–6.
[15] Majumder R. A hybrid microgrid with DC connection at back to back converters. IEEE Trans Smart Grid 2014;5:251–9.
[16] Zolfaghari M, Nurmanova V, Bagheri M, Gharehpetian GB. Adaptive gain-regulating-based control of parallel-connected Γ-Z-source power converters in hybrid microgrids. In: 2020 9th international conference on renewable energy research and application (ICRERA); 2020. p. 321–5.
[17] Xia Y, Wei W, Yu M, Wang X, Peng Y. Power management for a hybrid AC/DC microgrid with multiple subgrids. IEEE Trans Power Electron 2018;33:3520–33.
[18] Xiao H, Luo A, Shuai Z, Jin G, Huang Y. An improved control method for multiple bidirectional power converters in hybrid AC/DC microgrid. IEEE Trans Smart Grid 2016;7:340–7.
[19] Yu X, She X, Zhou X, Huang AQ. Power management for DC microgrid enabled by solid-state transformer. IEEE Trans Smart Grid 2014;5:954–65.
[20] Kumar C, Zou Z, Liserre M. Smart transformer-based hybrid grid loads support in partial disconnection of MV/HV power system. In: 2016 IEEE energy conversion congress and exposition (ECCE); 2016. p. 1–8.
[21] Eajal AA, Abdelwahed MA, El-Saadany EF, Ponnambalam K. A unified approach to the power flow analysis of AC/DC hybrid microgrids. IEEE Trans Sustainable Energy 2016;7:1145–58.
[22] Wang F, Duarte JL, Hendrix MAM. Grid-interfacing converter systems with enhanced voltage quality for microgrid application—concept and implementation. IEEE Trans Power Electron 2011;26:3501–13.
[23] Toodeji H, Fathi SH, Gharehpetian GB. Power management and performance improvement in integrated system of variable speed wind turbine and UPQC. In: 2009 International conference on clean electrical power; 2009. p. 609–14.
[24] Khorasani PG, Joorabian M, Seifossadat SG. Smart grid realization with introducing unified power quality conditioner integrated with DC microgrid. Electr Pow Syst Res 2017;151:68–85.
[25] Zolfaghari M, Abedi M, Gharehpetian GB. Power flow control of interconnected AC–DC microgrids in grid-connected hybrid microgrids using modified UIPC. IEEE Trans Smart Grid 2019;10:6298–307.
[26] Zolfaghari M, Abedi M, Gharehpetian GB. Power exchange control of clusters of multiple AC and DC microgrids interconnected by UIPC in hybrid microgrids. In: Electrical power distribution conference (EPDC); 2019. p. 22–6.
[27] Zolfaghari M, Ahmadiahangar R, Gharehpetian GB, Rosin A. State space-based modeling and identification of flexible loads in renewable energy integrated power systems. In: 2021 IEEE international conference on environment and electrical engineering and 2021 IEEE industrial and commercial power systems Europe (EEEIC/I&CPS Europe); 2021. p. 1–5.
[28] Hanane Hemi NKMS, Naamane Aziz. A new proposed shepherd model of a li-ion open circuit battery based on data fitting. HAL OpenScience 2019.
[29] Liu Z, Miao S, Wang W, Sun D. Comprehensive control scheme for an interlinking converter in a hybrid AC/DC microgrid. CSEE J Power Energy Syst 2021;7:719–29.